

RESEARCH ARTICLE

View Article Online  
View Journal | View Issue



Cite this: *Inorg. Chem. Front.*, 2023, 10, 6253

# A new infrared nonlinear optical material BaZnGeS<sub>4</sub> with a wide band gap and large nonlinear optical response†

Hongshan Wang, ‡<sup>a,b</sup> Xueting Pan, ‡<sup>a</sup> Wang Zhao, <sup>a,b</sup> Yu Chu \*<sup>a,b</sup> and Junjie Li \*<sup>a,b</sup>

Developing high-performance infrared (IR) nonlinear optical (NLO) materials is essential for modern laser technology, but challenging due to the competition of the NLO coefficient and band gap in the structure. Based on the “electronic structure engineering bucket effect” and systematic experimental investigations on the A<sup>II</sup>B<sup>II</sup>C<sup>IV</sup>D<sub>4</sub><sup>VI</sup> family, three new alkaline earth metal sulfides Mg<sub>0.6</sub>Cd<sub>1.4</sub>GeS<sub>4</sub>, CaCdGeS<sub>4</sub>, and BaZnGeS<sub>4</sub> have been developed. The compounds show a structural change from the *Pnma* (CaCdGeS<sub>4</sub>) to the *Fdd2* (BaZnGeS<sub>4</sub>) space group. Among them, BaZnGeS<sub>4</sub> exhibits a phase-matching NLO response of ~0.8× AGS, a wide band gap of 3.36 eV, and a high laser-induced damage threshold of ~5.4× AGS, achieving a good balance between the NLO response and band gap, which makes it an excellent IR NLO material. Theoretical calculations show that the NLO effects of BaZnGeS<sub>4</sub> originated from the [ZnS<sub>4</sub>] and [GeS<sub>4</sub>] NLO-active motifs. The results indicate that BaZnGeS<sub>4</sub> is a promising anti-laser damage IR NLO material and enriches the chemical diversity of the A<sup>II</sup>B<sup>II</sup>C<sup>IV</sup>D<sub>4</sub><sup>VI</sup> family.

Received 31st July 2023,  
Accepted 2nd September 2023

DOI: 10.1039/d3qi01502e

rsc.li/frontiers-inorganic

## Introduction

Nonlinear optical (NLO) crystals, as the critical optical devices of all-solid-state lasers, play a critical role in the development of coherent light sources through frequency-conversion technology, which shows wide applications in the fields of laser lithography, medical diagnostics, environmental monitoring, remote sensing, communication, and so on.<sup>1–3</sup> Over the past decades, borate-based NLO crystals, such as β-BaB<sub>2</sub>O<sub>4</sub>, LiB<sub>3</sub>O<sub>5</sub>, and KBe<sub>2</sub>BO<sub>3</sub>F<sub>2</sub>, have achieved great success in ultraviolet (UV) and deep-UV regions.<sup>4–9</sup> In IR regions, the commercially available IR NLO crystals AgGaS<sub>2</sub> (AGS), AgGaSe<sub>2</sub> (AGSe), and ZnGeP<sub>2</sub> (ZGP) show strong NLO responses,<sup>10–12</sup> but low laser-induced damage thresholds (LIDTs) (AGS/Se) or narrow band gap induced two-photon absorption around 1 μm (ZGP), which limits their further applications in modern laser technology.<sup>13–17</sup> Hence, the development of new IR NLO materials with wide band gaps and strong NLO responses is still a hot topic in this field.

For an excellent IR NLO material, the following requirements related to optical properties are highly expected: (i) a high NLO effect ≥0.5× AGS, preferably ≥1.0× AGS to improve the frequency conversion efficiency; (ii) a large band gap (*E<sub>g</sub>* > 3.0 eV) to prevent two-photon absorption around 1 μm and achieve high LIDT; (iii) a wide IR transparency range covering the two important IR atmospheric windows (3–5 μm and 8–12 μm); and (iv) moderate birefringence to meet the phase-matching (PM) condition.<sup>18–20</sup> To obtain a strong NLO response and wide IR transparent region, chalcogenides have been regarded as a promising system,<sup>21–26</sup> and to produce a wide band gap, introducing alkali and/or alkaline earth metal (AEM) without d–d and f–f electron transitions has been recognized as a feasible strategy.<sup>27–32</sup> Recently, the quaternary A<sup>II</sup>B<sup>II</sup>C<sup>IV</sup>D<sub>4</sub><sup>VI</sup> family compounds with abundant and adjustable structure sites have received considerable attention in the design of high-performance IR NLO materials.<sup>33</sup> However, most of the developed compounds in the A<sup>II</sup>B<sup>II</sup>C<sup>IV</sup>D<sub>4</sub><sup>VI</sup> family show narrow band gaps (≤3.0 eV).<sup>34</sup> Based on the “electronic structure engineering bucket effect” promoted by Chen *et al.*,<sup>35</sup> BaZnGeS<sub>4</sub> could be predicted as a promising wide band gap IR NLO material considering the wide band gaps of the involved binary phases (BaS: 3.88 eV; ZnS: 3.87 eV; GeS<sub>2</sub>: 3.54 eV) in the structure. Moreover, the A-site atom in this family is limited to Sr and Ba, and the number (~26, Table S1†) of A<sup>II</sup>B<sup>II</sup>C<sup>IV</sup>D<sub>4</sub><sup>VI</sup> family compounds is far less than the one (more than 38) of A<sub>2</sub><sup>I</sup>B<sup>II</sup>C<sup>IV</sup>D<sub>4</sub><sup>VI</sup> family compounds.<sup>34,36</sup>

<sup>a</sup>Research Center for Crystal Materials; CAS Key Laboratory of Functional Materials and Devices for Special Environments; Xinjiang Technical Institute of Physics & Chemistry, CAS, 40-1 South Beijing Road, Urumqi 830011, China.

E-mail: chuy@ms.xjb.ac.cn, lijunjie@ms.xjb.ac.cn

<sup>b</sup>Center of Materials Science and Optoelectronics Engineering, University of Chinese Academy of Sciences, Beijing 100049, China

†Electronic supplementary information (ESI) available. CCDC 2285773–2285775. For ESI and crystallographic data in CIF or other electronic format see DOI: <https://doi.org/10.1039/d3qi01502e>

‡These authors contributed equally to this work.

In this work, systematic experimental investigations were carried out on quaternary AEM-Zn/Cd-Ge-S systems, and three new AEM-containing sulfides  $\text{Mg}_{0.6}\text{Cd}_{1.4}\text{GeS}_4$ ,  $\text{CaCdGeS}_4$ , and  $\text{BaZnGeS}_4$  were synthesized through high-temperature solid-state reactions. The compounds show an interesting structural change from the centrosymmetric (CS) *Pnma* ( $\text{Mg}_{0.6}\text{Cd}_{1.4}\text{GeS}_4$  and  $\text{CaCdGeS}_4$ ) to the non-centrosymmetric (NCS) *Fdd2* ( $\text{BaZnGeS}_4$ ) space group. It is worth noting that  $\text{BaZnGeS}_4$  is composed of  $[\text{BaS}_8]$ ,  $[\text{ZnS}_4]$ , and  $[\text{GeS}_4]$  units and belongs to the  $A^{II}B^{IV}C^{IV}D_4^{VI}$  family, while  $\text{CaCdGeS}_4$  and  $\text{Mg}_{0.6}\text{Cd}_{1.4}\text{GeS}_4$  are isostructural compounds consisting of  $[\text{Ca}/\text{CdS}_6]/[\text{Mg}/\text{CdS}_6]$  and  $[\text{GeS}_4]$  units that are derived from the  $A_2^{II}C^{IV}D_4^{VI}$  family. Among them,  $\text{BaZnGeS}_4$  exhibits excellent optical properties including a large NLO response ( $\sim 0.8 \times \text{AgGaS}_2$ ), a high LIDT ( $5.4 \times \text{AgGaS}_2$ ), a wide experimental band gap ( $E_g = 3.36 \text{ eV}$ ), and a large birefringence ( $\Delta n_{\text{cal}} = 0.135@1064 \text{ nm}$ ), and could be a promising IR NLO material for high power IR lasers.

## Experimental section

### Materials

The high-purity starting materials BaS (99.99%), SrS (99.99%), CaS (99.99%), MgS (99.99%), Zn (99.99%), Cd (99.99%), Ge (99.99%), and S (99.99%), which are utilized for the experimental preparations, were purchased from the Aladdin website. To prevent the possible oxidation and deliquescence of sulfides, they were stored in dry argon-filled glove boxes.

### Chemical syntheses

The single crystals for structural determinations of  $\text{Mg}_{0.6}\text{Cd}_{1.4}\text{GeS}_4$ ,  $\text{CaCdGeS}_4$ , and  $\text{BaZnGeS}_4$  were prepared through high-temperature solid-state reactions. The starting mixtures of BaS/CaS/MgS, Zn/Cd, Ge, and S with stoichiometric ratios of 1 : 1 : 1 : 3 were weighed and loaded into quartz tubes with an inner diameter of 10 mm. After initial mixing, the samples were vacuumed to  $10^{-3} \text{ Pa}$  and then flame sealed. The sealed quartz tubes were placed in a muffle furnace with programmed temperature, slowly heated to 800 °C ( $\text{BaZnGeS}_4$ ) or 900 °C ( $\text{Mg}_{0.6}\text{Cd}_{1.4}\text{GeS}_4$ ,  $\text{CaCdGeS}_4$ ) at a speed of 6 °C  $\text{h}^{-1}$ , held for 60 h to complete the reactions, and then slowly cooled to room temperature at 8 °C  $\text{h}^{-1}$ . Finally, tablet-like  $\text{BaZnGeS}_4$ / $\text{CaCdGeS}_4$ / $\text{Mg}_{0.6}\text{Cd}_{1.4}\text{GeS}_4$  single crystals were harvested. The pure-phase powder samples of  $\text{BaZnGeS}_4$  and  $\text{Mg}_{0.6}\text{Cd}_{1.4}\text{GeS}_4$  were synthesized through similar procedures with the chemical stoichiometric ratios of BaS:Zn:Ge:S = 1:1:1:3 and MgS:Cd:Ge:S = 0.6:1.4:1:3.4, respectively, and the holding time at the reaction temperatures (800 °C for  $\text{BaZnGeS}_4$  and 900 °C for  $\text{Mg}_{0.6}\text{Cd}_{1.4}\text{GeS}_4$ ) was set to 100 h.

### Single crystal X-ray diffraction (XRD) measurements

The single-crystal XRD data of the three compounds were collected on a Bruker SMART APEX III CCD single-crystal X-ray diffractometer with Mo  $K_\alpha$  radiation ( $\lambda = 0.71073 \text{ \AA}$ ) at room temperature. The collected data of these crystals were integrated using the SAINT program and the multi-scan type

absorption correction of the structures was performed using the SADABS program, and then refined using the structure resolution program package SHELXL by full-matrix least-squares fitting on  $F^2$ .<sup>37,38</sup> In  $\text{BaZnGeS}_4$ , there is no atomic co-occupation. While in  $\text{Mg}_{0.6}\text{Cd}_{1.4}\text{GeS}_4$  and  $\text{CaCdGeS}_4$ , the Mg/Ca is co-occupied with Cd atoms at two crystallographically unique sites, owing to the similar cationic radii and coordination configurations of Mg/Ca and Cd. For a clearer ratio, based on free occupancy refinement initially, the occupancies of Mg/Cd were fixed to 0.1/0.9 for Mg(1)/Cd(1), 0.5/0.5 for Mg(2)/Cd(2) in  $\text{Mg}_{0.6}\text{Cd}_{1.4}\text{GeS}_4$ , and 0.8/0.2 for Ca(1)/Cd(1), 0.2/0.8 for Ca(2)/Cd(2) in  $\text{CaCdGeS}_4$ , respectively. The PLATON program was used to check the lacking symmetry elements and no higher symmetries were found.<sup>39</sup>

### Powder XRD (PXRD) characterization

The PXRD measurements were performed on a Bruker D2 PHASER diffractometer with Cu  $K_\alpha$  radiation ( $\lambda = 1.5418 \text{ \AA}$ ) at room temperature. The PXRD data were collected with the  $2\theta$  ranging from 10 to 70° and a scan step rate of 0.02°. The theoretical XRD patterns of  $\text{BaZnGeS}_4$  and  $\text{Mg}_{0.6}\text{Cd}_{1.4}\text{GeS}_4$  were obtained using Mercury software based on their CIF files.

### Energy-dispersive spectroscopy (EDS)

The EDS and mapping of  $\text{Mg}_{0.6}\text{Cd}_{1.4}\text{GeS}_4$ ,  $\text{CaCdGeS}_4$ , and  $\text{BaZnGeS}_4$  single crystals were performed on a field emission scanning electron microscope (FE-SEM, JEOL JSM-7610F Plus, Japan) equipped with an energy-dispersive spectrometer (Oxford, X-Max 50). It was operated at 5 kV.

### UV-vis-near-IR (NIR) diffuse-reflectance spectroscopy

The ultraviolet-visible-near infrared (UV-vis-NIR) diffuse-reflectance spectra of  $\text{BaZnGeS}_4$  and  $\text{Mg}_{0.6}\text{Cd}_{1.4}\text{GeS}_4$  polycrystalline powder samples were recorded on a ShimadzuSolidSpec-3700 DUV UV-Vis-IR spectrometer. The measurement range was from 200 to 2600 nm, and  $\text{BaSO}_4$  was used as the diffuse reflection standard. The diffuse reflection data were converted into absorption data using the Kubelka-Munk function  $F(R) = \alpha/S = (1 - R)^2/2R$ , where  $F(R)$  means the ratio of the absorption coefficient to the scattering coefficient;  $\alpha$ ,  $R$ , and  $S$  represent the absorption coefficient, reflectance, and scattering coefficient, respectively.

### Raman spectroscopy

Raman spectra of the three compounds in the 4000–100  $\text{cm}^{-1}$  region (2.5–100  $\mu\text{m}$ ) were recorded on a LABRAM HR Evolution spectrometer equipped with a CCD detector using 532 and 633 nm radiation from a diode laser. High-quality crystals of samples were selected and placed on a glass slide for measurement. The maximum power of the laser was set to 60 mW, and the data collection was completed within 15 s.

### Second-harmonic generation (SHG) measurements

The powder SHG responses of  $\text{BaZnGeS}_4$  were measured using the Kurtz-Perry method (It is widely applied for the evaluation of SHG response of a new NLO material.<sup>40–42</sup>) on a 2.09  $\mu\text{m}$  Q-switched laser, and the SHG signals were detected on a

photomultiplier tube and recorded using an oscilloscope. Before the experiments, the polycrystalline powder samples were ground and sieved in the range of  $\leq 45$ , 45–63, 63–90, 90–125, 125–180, and 180–212  $\mu\text{m}$ , respectively. Commercial AGS samples with the same particle size distribution were used as the references.

### Laser-induced damage threshold (LIDT) measurements

The LIDT of  $\text{BaZnGeS}_4$  micro-crystal samples was evaluated using the single-pulse LIDT method under a pulsed Nd: YAG laser (1.06  $\mu\text{m}$ , 9 ns, 1 Hz).<sup>43,44</sup> The AGS sample with a similar size ( $\leq 45$   $\mu\text{m}$ ) distribution was utilized as the reference. The laser output energy was gradually increased until the sample was damaged (color changed) on the surface. The damaging energies were found to be  $\sim 240$   $\mu\text{J}$  for  $\text{BaZnGeS}_4$  and  $\sim 45$   $\mu\text{J}$  for  $\text{AgGaS}_2$ . The LIDT of  $\text{BaZnGeS}_4$  samples can be derived as follows:

$$\begin{aligned} \text{LIDT}_{\text{BaZnGeS}_4} &= L_{\text{AGS}} \frac{\frac{E(\text{BaZnGeS}_4)}{\pi r^2 \tau_p}}{\frac{E(\text{AGS})}{\pi r^2 \tau_p}} \\ &= L_{\text{AGS}} \frac{E(\text{BaZnGeS}_4)}{E(\text{AGS})} \approx 5.4 \times \text{AGS} \end{aligned} \quad (1)$$

where  $E$  is the laser energy of a single pulse,  $r$  is the spot radius, and  $\tau_p$  is the pulse width.

### Computational descriptions

The electronic band structure, the density of states, and the optical properties of  $\text{BaZnGeS}_4$  were investigated using density functional theory (DFT) calculations in the CASTEP package.<sup>45</sup> To describe the exchange–correlation energy, the Perdew–Burke–Ernzerhof (PBE)<sup>46</sup> exchange–correlation of generalized gradient approximation (GGA)<sup>47</sup> was used for the calculations. The HSE06 band gap of  $\text{BaZnGeS}_4$  was investigated in PWmat code based on the Heyd–Scuseria–Ernzerhof (HSE06) hybrid functional with a plane wave cut off of 50 Ryd.<sup>48</sup> Meanwhile, the interaction between the ionic core and valence electrons was described using the norm-conserving pseudopotential (NCP).<sup>49</sup> The following valence-electron configurations were considered in the computation: Ba  $5s^2 5p^6 6s^2$ , Zn  $3d^{10} 4s^2$ , Ge  $4s^2 4p^2$ , and S  $3s^2 3p^4$  for  $\text{BaZnGeS}_4$ . Moreover, the kinetic energy cut-off was set to be 720.0 eV, and the Monkhorst–Pack  $k$ -point meshes of  $7 \times 7 \times 7$  with a density of 0.015  $\text{\AA}^{-1}$  in the Brillouin zone (BZ) were utilized.<sup>54</sup> The real part of the dielectric function  $\epsilon(\omega)$ , refractive index  $n$  and other linear optical properties were calculated according to the Kramers–Kronig transformation. Meanwhile, the SHG-density method was used to analyze the contributions of the orbitals or bands to the second-order susceptibility.

## Results and discussion

### Crystal structures

$\text{Mg}_{0.6}\text{Cd}_{1.4}\text{GeS}_4$ ,  $\text{CaCdGeS}_4$ , and  $\text{BaZnGeS}_4$  transparent crystals for single-crystal XRD were picked under an optical micro-

scope. The results of single-crystal XRD show that the three compounds crystallize in the orthorhombic system but in different space groups (Table S2†). Specifically,  $\text{BaZnGeS}_4$  belongs to the  $A''B''C^{IV}D_4^{VI}$  family and crystallizes in the  $Fdd2$  (No. 43) space group with cell parameters  $a = 21.0291(6)$   $\text{\AA}$ ,  $b = 21.7992(6)$   $\text{\AA}$ ,  $c = 12.3028(3)$   $\text{\AA}$ ,  $Z = 32$ . In its asymmetric unit, there are three crystallographically unique Ba (Ba (1), Ba (2), Wyckoff site  $8a$ ; Ba (3), Wyckoff site  $16b$ ), two Zn (Wyckoff site  $16b$ ), two Ge (Wyckoff site  $16b$ ), and eight S (Wyckoff site  $16b$ ) atoms. The Zn and Ge atoms are bonded to four S atoms to form tetrahedral  $[\text{ZnS}_4]$  units with the bond lengths  $d_{\text{Zn-S}} = 2.288$ – $2.403$   $\text{\AA}$ , and  $[\text{GeS}_4]$  units with  $d_{\text{Ge-S}} = 2.187$ – $2.225$   $\text{\AA}$ , respectively (Fig. 1a and b). The formed  $[\text{ZnS}_4]$  and  $[\text{GeS}_4]$  tetrahedral units are edge-sharing in a  $[\text{ZnGeS}_6]$  dimer (Fig. 1c) and further connected *via* corner-sharing to build the  $[\text{Zn}_3\text{Ge}_3\text{S}_{16}]_\infty$  layer in the  $ac$  and  $ab$  planes (Fig. 1e and f). Ba atoms are bound with eight S atoms to form  $[\text{BaS}_8]$  polyhedra with  $d_{\text{Ba-S}} = 3.188$ – $3.256$   $\text{\AA}$ , and the  $[\text{BaS}_8]$  polyhedra are further connected to form a channel-like three-dimensional (3D)  $[\text{BaS}_8]_\infty$  framework (Fig. 1d and g). The  $[\text{ZnS}_4]$  and  $[\text{GeS}_4]$  tetrahedra fill the channels to result in the final crystal structure of  $\text{BaZnGeS}_4$  (Fig. 1h).

Different from  $\text{BaZnGeS}_4$ ,  $\text{Mg}_{0.6}\text{Cd}_{1.4}\text{GeS}_4$  and  $\text{CaCdGeS}_4$  are isostructural compounds and crystallize in the  $Pnma$  space group (Table S2†). Since they show similar structure features (Fig. S1 and S2†),  $\text{CaCdGeS}_4$  is used as an example to illustrate their crystal structures here. In the asymmetric unit of  $\text{CaCdGeS}_4$ , there are two crystallographically independent M (Ca/Cd) (M (1), Wyckoff site  $4c$ ; M (2), Wyckoff site  $4b$ ), one Ge (Wyckoff site  $4c$ ), and three S (S (1), S (3), Wyckoff site  $4c$ ; S (2), Wyckoff site  $8d$ ) atoms. The Ge atoms are coordinated with four S atoms to form  $[\text{GeS}_4]$  tetrahedral units with  $d_{\text{Ge-S}} = 2.177$ – $2.234$   $\text{\AA}$  (Fig. S1a†). The  $[\text{GeS}_4]$  tetrahedral units are isolated from each other to construct the  $[\text{GeS}_4]_\infty$  pseudo-chain

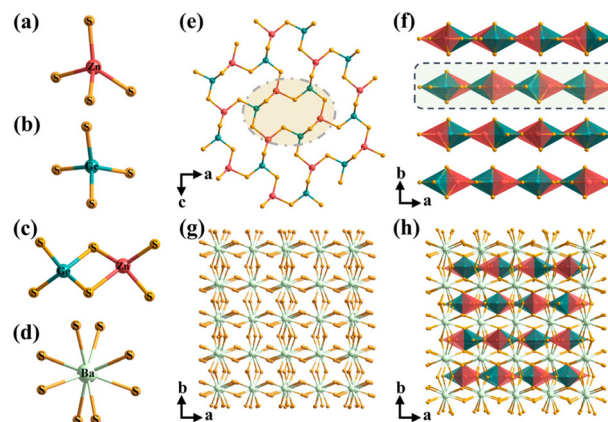


**Fig. 1** Crystal structure of  $\text{BaZnGeS}_4$ . (a, b and d) The coordination environments of Zn, Ge, and Ba atoms; (c) the formed  $[\text{ZnGeS}_6]$  dimer; (e and f) the formed 2D  $[\text{Zn}_3\text{Ge}_3\text{S}_{16}]_\infty$  layers with 12-membered rings viewed in the  $ac$  and  $ab$  planes; (g) the formed channel-like  $[\text{BaS}_8]_\infty$  framework; (h) the 3D crystal structure of  $\text{BaZnGeS}_4$  viewed along the  $c$  direction.



and  $[\text{GeS}_4]_\infty$  pseudo-layer structures in the *ac* and *ab* planes (Fig. S1d–f†), and the  $[\text{GeS}_4]$  units in each two adjacent  $[\text{GeS}_4]_\infty$  pseudo-chains (Fig. S1d and f†)/pseudo-layers (Fig. S1e†) show reverse arrangements. It is worth noting that the Ca/Cd occupancy at the M(1) site was refined to 0.5/0.5, while to 0.1/0.9 at the M(2) site. Different from the 8-coordinated Ba and 4-coordinated Zn in  $\text{BaZnGeS}_4$ , the Ca/Cd atoms are 6-coordinated with S atoms to form the  $[\text{Ca/CdS}_6]$  octahedral units, as shown in Fig. S1b and c.† The resulting  $[\text{Ca/Cd}(1)\text{S}_6]$  and  $[\text{Ca/Cd}(2)\text{S}_6]$  units are further linked by corner-sharing to build a 3D  $[\text{MS}_6]$  structural framework with channels, and the  $[\text{GeS}_4]$  units fill the channels to form the final crystal structure of  $\text{CaCdGeS}_4$  (Fig. S1g and h†).

Although  $\text{CaCdGeS}_4$  and  $\text{BaZnGeS}_4$  have a similar formula, their crystal structures are totally different, and  $\text{CaCdGeS}_4$  and  $\text{Mg}_{0.6}\text{Cd}_{1.4}\text{GeS}_4$  belong to the  $\text{A}_2^{\text{II}}\text{C}^{\text{IV}}\text{D}_4^{\text{VI}}$  family, rather than the  $\text{A}^{\text{II}}\text{B}^{\text{II}}\text{C}^{\text{IV}}\text{D}_4^{\text{VI}}$  family. To elucidate the structural difference in the two families, a detailed structure comparison was implemented, as shown in Fig. 2a–d. In  $\text{CaCdGeS}_4$  and  $\text{BaZnGeS}_4$ , the atomic coordination environments of Zn (coordination number: 4) and Cd (coordination number: 6) atoms and their connections with  $[\text{GeS}_4]$  tetrahedra are different. Moreover, there are 6 crystallographically unique atom sites in the asymmetric unit of  $\text{CaCdGeS}_4$  and 15 crystallographically unique atom sites in  $\text{BaZnGeS}_4$ , resulting in the degradation of structural symmetry from  $\text{CaCdGeS}_4$  to  $\text{BaZnGeS}_4$  (Fig. 2e and f).<sup>50</sup>

The computed bond valence sums (BVSS) (Ba: 2.31–2.32, Zn: 1.89–1.90, Ge: 4.02–4.05, and S: 2.01–2.14 in  $\text{BaZnGeS}_4$ ;

Mg/Cd: 2.11–2.18, Ge: 4.02, and S: 1.92–2.11 in  $\text{Mg}_{0.6}\text{Cd}_{1.4}\text{GeS}_4$ ; Ca/Cd: 2.20, Ge: 4.03, and S: 2.06–2.30 in  $\text{CaCdGeS}_4$ ) verify the reasonability of the crystal structures. The crystal data and structure refinement information, including atomic coordinates and equivalent isotropic displacement parameters, bond length, and angle information, are provided in the ESI (Tables S2–14†). To further confirm the compositions and chemical bonding in the three compounds, energy-dispersive X-ray spectroscopy (EDS) and Raman spectroscopy were performed. The EDS spectra and mapping confirm the presence and homogeneous distributions of Ba, Zn, Ge, and S elements in  $\text{BaZnGeS}_4$ , and Ca/Mg, Cd, Ge, and S elements in  $\text{CaCdGeS}_4/\text{Mg}_{0.6}\text{Cd}_{1.4}\text{GeS}_4$  (Fig. S3†). Meanwhile, the vibration peaks at 315.03 and 377.47  $\text{cm}^{-1}$  in  $\text{BaZnGeS}_4$ , 375.69  $\text{cm}^{-1}$  in  $\text{Mg}_{0.6}\text{Cd}_{1.4}\text{GeS}_4$ , and 370.75  $\text{cm}^{-1}$  in  $\text{CaCdGeS}_4$  can be attributed to the vibrations of Ge–S bonds; the peak at 244.93  $\text{cm}^{-1}$  in  $\text{BaZnGeS}_4$  (293.52  $\text{cm}^{-1}$  in  $\text{Mg}_{0.6}\text{Cd}_{1.4}\text{GeS}_4$  and 280.91  $\text{cm}^{-1}$  in  $\text{CaCdGeS}_4$ ) can be assigned to the vibrations of Zn–S (Cd–S) bonds (Fig. S4†).<sup>27,51–55</sup>

### Optical properties

To evaluate the optical properties,  $\text{BaZnGeS}_4$  and  $\text{Mg}_{0.6}\text{Cd}_{1.4}\text{GeS}_4$  polycrystalline powder samples were synthesized through conventional solid-state reactions at 800 and 900 °C, respectively. The experimental PXRD patterns of  $\text{BaZnGeS}_4$  and  $\text{Mg}_{0.6}\text{Cd}_{1.4}\text{GeS}_4$  matched well with the theoretical results derived from their Cif files (Fig. S5†), indicating high purity of the obtained polycrystalline samples. To detect the optical band gap, the UV-vis-NIR diffuse reflectance spectra of  $\text{BaZnGeS}_4$  and  $\text{Mg}_{0.6}\text{Cd}_{1.4}\text{GeS}_4$  were measured on the polycrystalline powder samples. Based on the Kubelka–Munk function,<sup>26,56,57</sup> the experimental band gaps of  $\text{BaZnGeS}_4$  and  $\text{Mg}_{0.6}\text{Cd}_{1.4}\text{GeS}_4$  are determined to be ~3.36 (Fig. 3a) and 2.94 eV (Fig. S6†). The band gap (3.36 eV) of  $\text{BaZnGeS}_4$  is far larger than the ones in commercial IR NLO materials such as AGS (2.73 eV), AGSe (1.83 eV), and ZGP (2.34 eV), and larger than the ones in most of the  $\text{A}^{\text{II}}\text{B}^{\text{II}}\text{C}^{\text{IV}}\text{D}_4^{\text{VI}}$  family compounds such as  $\text{BaZnSnS}_4$  (3.25 eV),<sup>58</sup>  $\text{SrZnSnS}_4$  (2.83 eV),<sup>59</sup>  $\beta\text{-BaHgSnS}_4$  (2.77 eV),<sup>60</sup> and  $\text{SrHgSnS}_4$  (2.72 eV).<sup>60</sup> It is comparable with the ones in the recently developed IR NLO compounds, such as  $[\text{Ba}_4(\text{S}_2)]_2[\text{ZnGa}_4\text{S}_{10}]$  (3.39 eV),<sup>55</sup>  $\text{AgAsS}_8$  (A = K, Rb, Cs) (3.23, 3.10, 3.37 eV),<sup>61</sup> and  $\text{Na}_2\text{Ba}[\text{Na}_2\text{Sn}_2\text{S}_7]$  (3.42 eV).<sup>62</sup> Generally, a wide band gap inherently contributes to a high LIDT,<sup>63–65</sup> and it was evaluated by the single-pulse LIDT method with AGS as the reference. The LIDT of  $\text{BaZnGeS}_4$  was found to be ~5.4 times that of AGS under the same test conditions (Fig. S7†).

Since  $\text{BaZnGeS}_4$  crystallizes in the NCS orthorhombic *Fdd2* space group, its SHG properties were evaluated using the Kurtz–Perry method under 2.09  $\mu\text{m}$  irradiation, and AGS samples were utilized as the references. As shown in Fig. 3b, the measured SHG response (180–212  $\mu\text{m}$ ) of  $\text{BaZnGeS}_4$  is about ~0.8× AGS. Meanwhile, the SHG intensities are increased with the particle sizes, implying that  $\text{BaZnGeS}_4$  is a phase-matching compound with 2.09  $\mu\text{m}$  pumping which is important for practical applications.<sup>57</sup> As shown in Fig. 3c, the

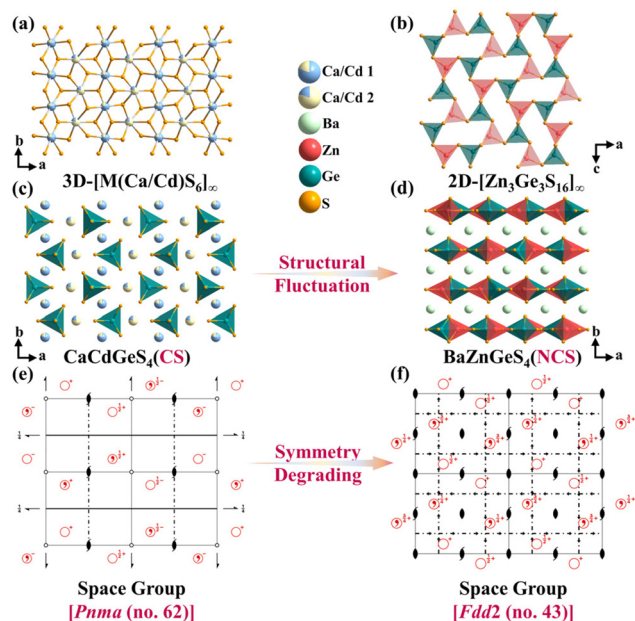


**Fig. 2** Structural difference in  $\text{CaCdGeS}_4$  and  $\text{BaZnGeS}_4$ . (a) The formed 6-coordinated  $[\text{Ca/CdS}_6]$  octahedra in  $\text{CaCdGeS}_4$ ; (b) the formed 4-coordinated  $[\text{ZnS}_4]$  tetrahedra in  $\text{BaZnGeS}_4$ ; (c and d) the crystal structures of  $\text{CaCdGeS}_4$  and  $\text{BaZnGeS}_4$  viewed along the *c* direction; (e and f) detailed spatial symmetry operations in  $\text{CaCdGeS}_4$  (*Pnma*) and  $\text{BaZnGeS}_4$  (*Fdd2*).

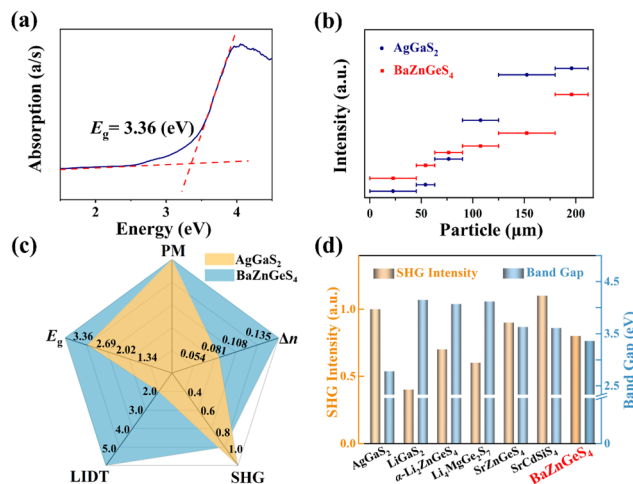


**Fig. 3** (a) Experimental band gap of BaZnGeS<sub>4</sub>; (b) the SHG intensities versus particle sizes with AGS as the references under 2.09 μm irradiation; (c) the comparison of optical properties between BaZnGeS<sub>4</sub> and benchmark AGS; (d) the typical alkali- and/or AEM-containing sulfide IR NLO candidates with PM behavior, AGS is used as the reference.

experimental results indicate that BaZnGeS<sub>4</sub> achieves a good balance between a wide band gap ( $E_g \geq 3.0$  eV) and large SHG response ( $\geq 0.5 \times$  AGS) for an anti-laser damage IR NLO material,<sup>22,66–68</sup> which are comparable with those of typical alkali- and/or AEM-containing sulfide IR NLO materials developed recently, such as LiGaS<sub>2</sub>,<sup>69</sup> α-Li<sub>2</sub>ZnGeS<sub>4</sub>,<sup>70</sup> Li<sub>4</sub>MgGe<sub>2</sub>S<sub>7</sub>,<sup>52</sup> SrZnGeS<sub>4</sub>,<sup>34</sup> and SrCdSiS<sub>4</sub><sup>71</sup> (Fig. 3d).

### Theoretical calculations

To clarify the origin of the optical properties, the electronic structure of BaZnGeS<sub>4</sub> was calculated using the first-principles calculations based on DFT.<sup>72–75</sup> The calculated band structure (Fig. 4a) shows that BaZnGeS<sub>4</sub> has a direct band gap of 2.71 eV, which is smaller than the experimental value due to the discontinuity of exchange–correlation energy of the GGA.<sup>76,77</sup> Hence, the HSE06 band gap is investigated,<sup>78,79</sup> and the calculated HSE06 band gap of BaZnGeS<sub>4</sub> is about 3.52 eV, which matches with the experimental result (3.36 eV), illustrating the reliability of the HSE06 hybrid functional. Moreover, the top of the valence band (VB) of BaZnGeS<sub>4</sub> is mainly occupied by the S 3p, Ge 4s, and Zn 4s orbitals, while the bottom of the conduction band (CB) is primarily composed of S 3p, Ge 4p, and Zn 4s orbitals (Fig. 4b), indicating that the optical band gap of BaZnGeS<sub>4</sub> is mainly determined by the [GeS<sub>4</sub>] and [ZnS<sub>4</sub>] tetrahedral units.

To evaluate the birefringence of the title compound, the refractive indices along the optical axes ( $n_x$ ,  $n_y$ ,  $n_z$ ) were computed. As shown in Fig. S8a,† the dielectric constants of BaZnGeS<sub>4</sub> show the trends of  $n_z > n_y > n_x$  and  $n_z - n_y > n_y - n_x$ . It means that BaZnGeS<sub>4</sub> is a negative biaxial crystal. The calculated birefringence of BaZnGeS<sub>4</sub> is 0.135@1064 nm (Fig. S8b†), which matches the PM behavior, as shown in Fig. 3b. The large birefringence could be related to the formed

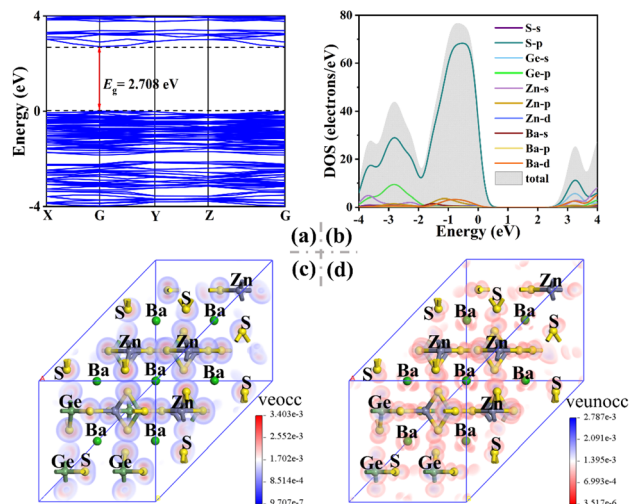


**Fig. 4** (a) Band structure; (b) the density of states (DOS) and partial DOS; (c and d) the SHG-density maps of the occupied (c) and unoccupied (d) orbitals in the virtual-electron process of BaZnGeS<sub>4</sub>.

[Zn<sub>3</sub>Ge<sub>3</sub>S<sub>16</sub>]<sub>∞</sub> layers with large optical anisotropy in the structure. To uncover the origin of the NLO effect in BaZnGeS<sub>4</sub>, the SHG density maps of occupied (Fig. 4c) and unoccupied (Fig. 4d) states in the virtual-electron (VE) process were calculated. The results confirm that [ZnS<sub>4</sub>] and [GeS<sub>4</sub>] units make significant contributions to the SHG responses.

## Conclusions

In conclusion, three new AEM-containing sulfides, Mg<sub>0.6</sub>Cd<sub>1.4</sub>GeS<sub>4</sub>, CaCdGeS<sub>4</sub>, and BaZnGeS<sub>4</sub> with a structural change from the CS *Pnma* (Mg<sub>0.6</sub>Cd<sub>1.4</sub>GeS<sub>4</sub> and CaCdGeS<sub>4</sub>) to the NCS *Fdd2* (BaZnGeS<sub>4</sub>) space group, have been successfully synthesized through conventional solid-state reactions. Among them, BaZnGeS<sub>4</sub> belongs to the A<sup>II</sup>B<sup>II</sup>C<sup>IV</sup>D<sub>4</sub><sup>VI</sup> family, and Mg<sub>0.6</sub>Cd<sub>1.4</sub>GeS<sub>4</sub> and CaCdGeS<sub>4</sub> are isostructural compounds belonging to the A<sub>2</sub><sup>II</sup>C<sup>IV</sup>D<sub>4</sub><sup>VI</sup> family. Based on the “electronic structure engineering bucket effect”, BaZnGeS<sub>4</sub> exhibits a wide band gap of 3.36 eV, larger than most of the values for the A<sup>II</sup>B<sup>II</sup>C<sup>IV</sup>D<sub>4</sub><sup>VI</sup> family compounds. Meanwhile, it has a large SHG response ( $\sim 0.8 \times$  AGS), a large birefringence ( $\Delta n_{\text{cal}} = 0.135@1064$  nm), and a high LIDT (5.4× AGS). It could be a promising anti-laser damage IR NLO candidate. The theoretical calculations indicate that the optical band gap and SHG response in BaZnGeS<sub>4</sub> mainly stem from the NLO-active [ZnS<sub>4</sub>] and [GeS<sub>4</sub>] tetrahedral units. The results verify the feasibility of designing wide band gap chalcogenides using the “electronic structure engineering bucket effect”.

## Conflicts of interest

The authors declare that they have no conflict of interest.

## Acknowledgements

This work was supported by the High-level Talent Project of Xinjiang Uygur Autonomous Region (2020000039), the National Natural Science Foundation of China (52002398, 61835014, and 51972336), the West Light Foundation of the CAS (2019-YDYLT002), and the Xinjiang Key Laboratory of Electronic Information Materials and Devices (2017D04029).

## References

- G. Shi, Y. Wang, F. Zhang, B. Zhang, Z. Yang, X. Hou, S. Pan and K. R. Poeppelmeier, Finding the next deep-ultraviolet nonlinear optical material:  $\text{NH}_4\text{B}_4\text{O}_6\text{F}$ , *J. Am. Chem. Soc.*, 2017, **139**, 10645–10648.
- J. Li and F. L. Deepak, In situ kinetic observations on crystal nucleation and growth, *Chem. Rev.*, 2022, **122**, 16911–16982.
- L. Qi, Z. Chen, X. Shi, X. Zhang, Q. Jing, N. Li, Z. Jiang, B. Zhang and M. Lee,  $\text{A}_3\text{BBi}(\text{P}_2\text{O}_7)_2$  ( $\text{A} = \text{Rb}, \text{Cs}$ ;  $\text{B} = \text{Pb}, \text{Ba}$ ): isovalent cation substitution to sustain large second-harmonic generation responses, *Chem. Mater.*, 2020, **32**, 8713–8723.
- B. Zhang, G. Shi, Z. Yang, F. Zhang and S. Pan, Fluorooxoborates: beryllium-free deep-ultraviolet nonlinear optical materials without layered growth, *Angew. Chem., Int. Ed.*, 2017, **56**, 3916–3919.
- S. Zhao, L. Kang, Y. Shen, X. Wang, M. A. Asghar, Z. Lin, Y. Xu, S. Zeng, M. Hong and J. Luo, Designing a beryllium-free deep-ultraviolet nonlinear optical material without a structural instability problem, *J. Am. Chem. Soc.*, 2016, **138**, 2961–2964.
- G. Zou and K. M. Ok, Novel ultraviolet (UV) nonlinear optical (NLO) materials discovered by chemical substitution-oriented design, *Chem. Sci.*, 2020, **11**, 5404–5409.
- M. Mutailipu, K. R. Poeppelmeier and S. Pan, Borates: a rich source for optical materials, *Chem. Rev.*, 2021, **121**, 1130–1202.
- Y. Long, X. Dong, L. Huang, H. Zeng, Z. Lin, L. Zhou and G. Zou,  $\text{BaSb}(\text{H}_2\text{PO}_4)_3\text{Cl}_2$ : an excellent UV nonlinear optical hypophosphite exhibiting strong second-harmonic generation response, *Mater. Today Phys.*, 2022, **28**, 100876.
- F. Hou, D. Mei, M. Xia and Y. Wu, Structure-performance relationship in tri-coordinated nonlinear optical materials toward optimal second harmonic generation and phase matching, *Coord. Chem. Rev.*, 2021, **444**, 214038.
- J. Chen, Q. Wu, H. Tian, X. Jiang, F. Xu, X. Zhao, Z. Lin, M. Luo and N. Ye, Uncovering a vital band gap mechanism of pnictides, *Adv. Sci.*, 2022, **9**, 2105787.
- J. Chen, H. Chen, F. Xu, L. Cao, X. Jiang, S. Yang, Y. Sun, X. Zhao, C. Lin and N. Ye,  $\text{Mg}_2\text{In}_3\text{Si}_2\text{P}_7$ : a quaternary diamond-like phosphide infrared nonlinear optical material derived from  $\text{ZnGeP}_2$ , *J. Am. Chem. Soc.*, 2021, **143**, 10309–10316.
- X. Chen, H. Jo and K. M. Ok, Lead mixed oxyhalides satisfying all fundamental requirements for high-performance mid-infrared nonlinear optical materials, *Angew. Chem., Int. Ed.*, 2020, **59**, 7514–7520.
- S. Yang, C. Lin, K. Chen, H. Fan, J. Chen, S. Fang, N. Ye and M. Luo, Trade-off for better balanced nonlinear optical performance with disordered Si in  $\text{ZnGeP}_2$ , *Chem. Mater.*, 2022, **34**, 11007–11013.
- A. Abudurusuli, J. Li and S. Pan, A review on the recently developed promising infrared nonlinear optical materials, *Dalton Trans.*, 2021, **50**, 3155–3160.
- J. Zhang, S. S. Stoyko, A. J. Craig, P. Grima, J. W. Kotchey, J. Jang and J. A. Aitken, Phase matching, strong frequency doubling, and outstanding laser-induced damage threshold in the biaxial, quaternary diamond-like semiconductor  $\text{Li}_4\text{CdSn}_2\text{S}_7$ , *Chem. Mater.*, 2020, **32**, 10045–10054.
- J. Li, W. Yao, J. Li, X. Li, W. Liu and S. Guo, Partial substitution induced structural transformation and enhanced nonlinear optical properties of  $\text{Na}_2\text{Ga}_x\text{In}_{6-x}\text{Se}_{10}$  ( $x = 3, 3.76$ ), *Mater. Today Phys.*, 2023, **32**, 101007.
- M. Mutailipu, J. Han, Z. Li, F. Li, J. Li, F. Zhang, X. Long, Z. Yang and S. Pan, Achieving the full-wavelength phase-matching for efficient nonlinear optical frequency conversion in  $\text{C}(\text{NH}_2)_3\text{BF}_4$ , *Nat. Photonics*, 2023, **17**, 694–701.
- Y. Guo, F. Liang, W. Yin, Z. Li, X. Luo, Z.-S. Lin, J. Yao, A. Mar and Y. Wu,  $\text{BaHgGeSe}_4$  and  $\text{SrHgGeSe}_4$ : two new Hg-Based infrared nonlinear optical materials, *Chem. Mater.*, 2019, **31**, 3034–3040.
- Y. Chu, P. Wang, H. Zeng, S. Cheng, X. Su, Z. Yang, J. Li and S. Pan,  $\text{Hg}_3\text{P}_2\text{S}_8$ : a new promising infrared nonlinear optical material with a large second-harmonic generation and a high laser-induced damage threshold, *Chem. Mater.*, 2021, **33**, 6514–6521.
- Y. Chu, H. Wang, T. Abutukadi, Z. Li, M. Mutailipu, X. Su, Z. Yang, J. Li and S. Pan,  $\text{Zn}_2\text{HgP}_2\text{S}_8$ : a wide bandgap Hg-Based infrared nonlinear optical material with large second-harmonic generation response, *Small*, 2023, 2305074, DOI: [10.1002/sml.202305074](https://doi.org/10.1002/sml.202305074).
- J. Zhou, L. Wang, Y. Chu, H. Wang, S. Pan and J. Li,  $\text{Na}_3\text{Si}_3\text{F}$ : a wide bandgap fluorothiosilicate with unique  $[\text{Si}_3\text{F}]$  unit and high laser-induced damage threshold, *Adv. Opt. Mater.*, 2023, 2300736, DOI: [10.1002/adom.202300736](https://doi.org/10.1002/adom.202300736).
- C. Li, X. Meng, Z. Li and J. Yao, Hg-based chalcogenides: an intriguing class of infrared nonlinear optical materials, *Coord. Chem. Rev.*, 2022, **453**, 214328.
- H. Liu, Z. Song, H. Wu, Z. Hu, J. Wang, Y. Wu and H. Yu,  $[\text{Ba}_2\text{F}_2][\text{Ge}_2\text{O}_3\text{S}_2]$ : an unprecedented heteroanionic infrared nonlinear optical material containing three typical anions, *ACS Mater. Lett.*, 2022, **4**, 1593–1598.
- D. Mei, W. Cao, N. Wang, X. Jiang, J. Zhao, W. Wang, J. Dang, S. Zhang, Y. Wu, P. Rao and Z. Lin, Breaking through the “3.0 eV wall” of energy band gap in mid-infra-



- red nonlinear optical rare earth chalcogenides by charge-transfer engineering, *Mater. Horiz.*, 2021, **8**, 2330–2334.
- 25 W. Wang, D. Mei, F. Liang, J. Zhao, Y. Wu and Z. Lin, Inherent laws between tetrahedral arrangement pattern and optical performance in tetrahedron-based mid-infrared nonlinear optical materials, *Coord. Chem. Rev.*, 2020, **421**, 213444.
  - 26 X. Gao, Q. Chen, Q. Qin, L. Li, M. Liu, D. Hao, J. Li, J. Li, Z. Wang and Z. Chen, Realization of flexible in-memory computing in a van der Waals ferroelectric heterostructure tri-gate transistor, *Nano Res.*, 2023, DOI: [10.1007/s12274-023-5964-8](https://doi.org/10.1007/s12274-023-5964-8).
  - 27 M. Mutailipu, M. Zhang, B. Zhang, L. Wang, Z. Yang, X. Zhou and S. Pan,  $\text{SrB}_5\text{O}_7\text{F}_3$  functionalized with  $[\text{B}_5\text{O}_9\text{F}_3]^{6-}$  chromophores: accelerating the rational design of deep-ultraviolet nonlinear optical materials, *Angew. Chem., Int. Ed.*, 2018, **57**, 6095–6099.
  - 28 Y. Song, S. Cui, Z. Qian, H. Yu, Z. Hu, J. Wang, Y. Wu and H. Wu,  $[\text{ASr}_4\text{Cl}][\text{Ge}_3\text{S}_{10}]$  ( $\text{A} = \text{Na}, \text{K}$ ) and  $[\text{KBa}_4\text{Cl}][\text{Ge}_3\text{S}_{10}]$ : new salt-inclusion infrared nonlinear optical crystals with zero-dimensional  $[\text{Ge}_3\text{S}_9]$  clusters, *Inorg. Chem. Front.*, 2022, **9**, 5932–5940.
  - 29 B. Liu, X. Jiang, H. Zeng and G. Guo,  $[\text{ABa}_2\text{Cl}][\text{Ga}_4\text{S}_8]$  ( $\text{A} = \text{Rb}, \text{Cs}$ ): wide-spectrum nonlinear optical materials obtained by polycation-substitution-induced nonlinear optical (NLO)-functional motif ordering, *J. Am. Chem. Soc.*, 2020, **142**, 10641–10645.
  - 30 J. Xu, K. Wu, B. Zhang, H. Yu and H. Zhang,  $\text{LaAeAl}_3\text{S}_7$  ( $\text{Ae} = \text{Ca}, \text{Sr}$ ): Cairo pentagonal layered thioaluminates achieving a good balance between a strong second harmonic generation response and a wide bandgap, *Inorg. Chem. Front.*, 2023, **10**, 2045–2052.
  - 31 Z. Qian, H. Liu, Y. Zhang, H. Wu, Z. Hu, J. Wang, Y. Wu and H. Yu, The exploration of new infrared nonlinear optical crystals based on the polymorphism of  $\text{BaGa}_4\text{S}_7$ , *Inorg. Chem. Front.*, 2022, **9**, 4632–4641.
  - 32 M. Zhang, N. Liang, D. Hao, Z. Chen, F. Zhang, J. Yin, Y. Yang and L. Yang, Recent advances of  $\text{SiO}_x$ -based anodes for sustainable lithium-ion batteries, *Nano Res. Energy*, 2023, **2**, e9120077.
  - 33 H. Lin, W. Wei, H. Chen, X. Wu and Q. Zhu, Rational design of infrared nonlinear optical chalcogenides by chemical substitution, *Coord. Chem. Rev.*, 2020, **406**, 213150.
  - 34 H. Chen, W. Wei, H. Lin and X. Wu, Transition-metal-based chalcogenides: A rich source of infrared nonlinear optical materials, *Coord. Chem. Rev.*, 2021, **448**, 214154.
  - 35 Q. Liu, X. Liu, L. Wu and L. Chen,  $\text{SrZnGeS}_4$ : a dual-wave-band nonlinear optical material with a transparency spanning UV/Vis and far-IR spectral regions, *Angew. Chem., Int. Ed.*, 2022, **61**, e202205587.
  - 36 G. Li, Z. Yang, J. Li and S. Pan, A review of the  $\text{A}_2\text{I}^{\text{II}}\text{B}^{\text{II}}\text{C}^{\text{IV}}\text{D}_4^{\text{VI}}$  family as infrared nonlinear optical materials: the effect of each site on the structure and optical properties, *Chem. Commun.*, 2020, **56**, 11565–11576.
  - 37 G. M. Sheldrick, A short history of SHELX, *Acta Crystallogr., Sect. A: Found. Crystallogr.*, 2008, **64**, 112–122.
  - 38 O. V. Dolomanov, L. J. Bourhis, R. J. Gildea, J. A. K. Howard and H. Puschmann, OLEX2: a complete structure solution, refinement and analysis program, *J. Appl. Crystallogr.*, 2009, **42**, 339–341.
  - 39 A. L. Spek, Single-crystal structure validation with the program PLATON, *J. Appl. Crystallogr.*, 2003, **36**, 7–13.
  - 40 L. Luo, L. Wang, J. Chen, J. Zhou, Z. Yang, S. Pan and J. Li,  $\text{A}^{\text{I}}\text{B}_3^{\text{II}}\text{C}_3^{\text{III}}\text{Q}_8^{\text{VI}}$ : a new family for the design of infrared nonlinear optical materials by coupling octahedra and tetrahedra units, *J. Am. Chem. Soc.*, 2022, **144**, 21916–21925.
  - 41 W. Cai, A. Abudurusuli, C. Xie, E. Tikhonov, J. Li, S. Pan and Z. Yang, Toward the rational design of mid-infrared nonlinear optical materials with targeted properties via a multi-level data-driven approach, *Adv. Funct. Mater.*, 2022, **32**, 2200231.
  - 42 X. Wang, Y. Wang, B. Zhang, F. Zhang, Z. Yang and S. Pan,  $\text{CsBa}_4\text{O}_6\text{F}$ : a congruent-melting deep-ultraviolet nonlinear optical material by combining superior functional units, *Angew. Chem., Int. Ed.*, 2017, **56**, 14119–14123.
  - 43 W. Chen, B. Liu, S. Pei, X. Jiang and G. Guo,  $[\text{K}_2\text{Pb}_X][\text{Ga}_7\text{S}_{12}]$  ( $\text{X} = \text{Cl}, \text{Br}, \text{I}$ ): the first lead-containing cationic moieties with ultrahigh second-harmonic generation and band gaps exceeding the criterion of 2.33 eV, *Adv. Sci.*, 2023, **10**, 2207630, DOI: [10.1002/advs.202207630](https://doi.org/10.1002/advs.202207630).
  - 44 P. Li, C. Hu, F. Kong and J. Mao, The first UV nonlinear optical selenite material: fluorination control in  $\text{CaYF}(\text{SeO}_3)_2$  and  $\text{Y}_3\text{F}(\text{SeO}_3)_4$ , *Angew. Chem., Int. Ed.*, 2023, **62**, e202301420.
  - 45 C. Bai, Y. Chu, J. Zhou, L. Wang, L. Luo, S. Pan and J. Li, Two new tellurite halides with cationic layers: syntheses, structures, and characterizations of  $\text{CdPb}_2\text{Te}_3\text{O}_8\text{Cl}_2$  and  $\text{Cd}_{13}\text{Pb}_8\text{Te}_{14}\text{O}_{42}\text{Cl}_{14}$ , *Inorg. Chem. Front.*, 2022, **9**, 1023–1030.
  - 46 A. M. Rappe, K. M. Rabe, E. Kaxiras and J. D. Joannopoulos, Optimized pseudopotentials, *Phys. Rev. B: Condens. Matter Mater. Phys.*, 1990, **41**, 1227–1230.
  - 47 J. P. Perdew, K. Burke and M. Ernzerhof, Generalized gradient approximation made simple, *Phys. Rev. Lett.*, 1996, **77**, 3865–3868.
  - 48 M. Hu, N. Tuerhong, Z. Chen, Q. Jing and M. Lee,  $\text{Li}_3\text{B}_8\text{O}_{13}\text{X}$  ( $\text{X} = \text{Cl}$  and  $\text{Br}$ ): two new noncentrosymmetric crystals with large birefringence induced by  $\text{BO}_3$  units, *Inorg. Chem.*, 2023, **62**, 3609–3615.
  - 49 D. R. Hamann, M. Schlüter and C. Chiang, Norm-Conserving Pseudopotentials, *Phys. Rev. Lett.*, 1979, **43**, 1494–1497.
  - 50 Y. Wang, M. L. Nisbet, K. R. Kamp, E. Hiralal, R. Gautier, P. S. Halasyamani and K. R. Poeppelmeier, Beyond  $\pi$ - $\pi$  stacking: understanding inversion symmetry breaking in crystalline racemates, *J. Am. Chem. Soc.*, 2023, **145**, 16879–16888.
  - 51 G. Li, Q. Liu, K. Wu, Z. Yang and S. Pan,  $\text{Na}_2\text{CdGe}_2\text{Q}_6$  ( $\text{Q} = \text{S}, \text{Se}$ ): two metal-mixed chalcogenides with phase-match-

- ing abilities and large second-harmonic generation responses, *Dalton Trans.*, 2017, **46**, 2778–2784.
- 52 A. Abudurusuli, J. Huang, P. Wang, Z. Yang, S. Pan and J. Li,  $\text{Li}_4\text{MgGe}_2\text{S}_7$ : the first alkali and alkaline-earth diamond-like infrared nonlinear optical material with exceptional large band gap, *Angew. Chem., Int. Ed.*, 2021, **60**, 24131–24136.
  - 53 G. Li, K. Wu, Q. Liu, Z. Yang and S. Pan,  $\text{Na}_2\text{ZnGe}_2\text{S}_6$ : a new infrared nonlinear optical material with good balance between large second-harmonic generation response and high laser damage threshold, *J. Am. Chem. Soc.*, 2016, **138**, 7422–7428.
  - 54 K. Wu and S. Pan,  $\text{Li}_2\text{HgMS}_4$  ( $\text{M} = \text{Si, Ge, Sn}$ ): new quaternary diamond-like semiconductors for infrared laser frequency conversion, *Crystals*, 2017, **7**, 107.
  - 55 K. Ding, H. Wu, Z. Hu, J. Wang, Y. Wu and H. Yu,  $[\text{Ba}_4(\text{S}_2)][\text{ZnGa}_4\text{S}_{10}]$ : design of an unprecedented infrared nonlinear salt-inclusion chalcogenide with disulfide bonds, *Small*, 2023, DOI: [10.1002/smll.202302819](https://doi.org/10.1002/smll.202302819).
  - 56 H. Zhou, L. Xiong, L. Chen and L. Wu, Dislocations that decrease size mismatch within the lattice leading to ultra-wide band gap, large second-order susceptibility, and high nonlinear optical performance of  $\text{AgGaS}_2$ , *Angew. Chem., Int. Ed.*, 2019, **58**, 9979–9983.
  - 57 G. Zou, C. Lin, H. Jo, G. Nam, T. S. You and K. M. Ok,  $\text{Pb}_2\text{BO}_3\text{Cl}$ : a tailor-made polar lead borate chloride with very strong second harmonic generation, *Angew. Chem., Int. Ed.*, 2016, **55**, 12078–12082.
  - 58 Y. Li, Z. Chen, W. Yao, R. Tang and S. Guo, Heterovalent cations substitution to design asymmetric chalcogenides with promising nonlinear optical performances, *J. Mater. Chem. C*, 2021, **9**, 8659–8665.
  - 59 Y. Zhang, D. Mei, Y. Yang, W. Cao, Y. Wu, J. Lu and Z. Lin, Rational design of a new chalcogenide with good infrared nonlinear optical performance:  $\text{SrZnSnS}_4$ , *J. Mater. Chem. C*, 2019, **7**, 8556–8561.
  - 60 Y. Guo, F. Liang, Z. Li, W. Xing, Z. Lin, J. Yao, A. Mar and Y. Wu,  $\text{AHgSnQ}_4$  ( $\text{A} = \text{Sr, Ba}$ ;  $\text{Q} = \text{S, Se}$ ): a series of Hg-Based infrared nonlinear-optical materials with strong second-harmonic-generation response and good phase matchability, *Inorg. Chem.*, 2019, **58**, 10390–10398.
  - 61 W. Chen, X. Jiang, S. Pei, M. Zhang, B. Liu and G. Guo, Ternary  $\text{AGa}_5\text{S}_8$  ( $\text{A} = \text{K, Rb, Cs}$ ): promising infrared nonlinear optical materials rationally realized by “one-for-multiple substitution” strategy, *Sci. China Mater.*, 2022, **66**, 740–747.
  - 62 R. Li, Q. Liu, X. Liu, Y. Liu, X. Jiang, Z. Lin, F. Jia, L. Xiong, L. Chen and L. Wu,  $\text{Na}_2\text{Ba}[\text{Na}_2\text{Sn}_2\text{S}_7]$ : Structural tolerance factor-guided NLO performance improvement, *Angew. Chem., Int. Ed.*, 2023, **62**, e202218048.
  - 63 M. Zhang, B. Liu, X. Jiang and G. Guo, Nonlinear optical sulfides  $\text{LiMGa}_8\text{S}_{14}$  ( $\text{M} = \text{Rb/Ba, Cs/Ba}$ ) created by  $\text{Li}^+$  driven 2D centrosymmetric to 3D noncentrosymmetric transformation, *Small*, 2023, **19**, 2302088.
  - 64 B. Liu, X. Jiang, B. Li, H. Zeng and G. Guo,  $[\text{LiCs}_2\text{Cl}][\text{Ga}_3\text{S}_6]$ : a nanoporous framework of  $\text{GaS}_4$  tetrahedra with excellent nonlinear optical performance, *Angew. Chem., Int. Ed.*, 2020, **59**, 4856–4859.
  - 65 Z. Wang, B. Liu and G. Guo, First polar quaternary sulphide  $\text{CsLiGa}_6\text{S}_{10}$  with mixed ordered alkali cations displaying excellent infrared nonlinear optical properties, *Inorg. Chem. Front.*, 2022, **9**, 6554–6560.
  - 66 H. Yang, M. Ran, W. Wei, X. Wu, H. Lin and Q. Zhu, Recent advances in IR nonlinear optical chalcogenides with well-balanced comprehensive performance, *Mater. Today Phys.*, 2023, **35**, 101127.
  - 67 Y. Song, Z. Qian, B. Zhou, H. Yu, Z. Hu, J. Wang, Y. Wu and H. Wu, A non-centrosymmetric chalcohalide synthesized through the combination of chemical tailoring with aliovalent substitution, *Chem. Commun.*, 2023, **59**, 3309–3312.
  - 68 J. Li, X. Li, W. Yao, W. Liu and S. Guo, Three-in-One strategy constructing the first high-performance nonlinear optical sulfide crystallizing with the  $P4_3$  space group, *Small*, 2023, DOI: [10.1002/smll.202303090](https://doi.org/10.1002/smll.202303090).
  - 69 L. Isaenko, A. Yelisseyev, S. Lobanov, A. Titov, V. Petrov, J. J. Zondy, P. Krinitsin, A. Merkulov, V. Vedenyapin and J. Smirnova, Growth and properties of  $\text{LiGaX}_2$  ( $\text{X} = \text{S, Se, Te}$ ) single crystals for nonlinear optical applications in the mid-IR, *Cryst. Res. Technol.*, 2003, **38**, 379–387.
  - 70 J. Zhang, D. J. Clark, J. A. Brant, K. A. Rosmus, P. Grima, J. W. Lekse, J. I. Jang and J. A. Aitken,  $\alpha\text{-Li}_2\text{ZnGeS}_4$ : a wide-bandgap diamond-like semiconductor with excellent balance between laser-induced damage threshold and second harmonic generation response, *Chem. Mater.*, 2020, **32**, 8947–8955.
  - 71 H. Yang, M. Ran, S. Zhou, X. Wu, H. Lin and Q. Zhu, Rational design via dual-site aliovalent substitution leads to an outstanding IR nonlinear optical material with well-balanced comprehensive properties, *Chem. Sci.*, 2022, **13**, 10725–10733.
  - 72 J. Yu, B. Zhang, X. Zhang, Y. Wang, K. Wu and M. Lee, Finding optimal mid-infrared nonlinear optical materials in germanates by first-principles high-throughput screening and experimental verification, *ACS Appl. Mater. Interfaces*, 2020, **12**, 45023–45035.
  - 73 Y. Wang, B. Zhang, Z. Yang and S. Pan, Cation-tuned synthesis of fluorooxoborates: towards optimal deep-ultraviolet nonlinear optical materials, *Angew. Chem., Int. Ed.*, 2018, **57**, 2150–2154.
  - 74 J. Zhang, R. Wei, D. Yang, Y. Wang and B. Zhang, Searching for silicate nonlinear optical materials by combining calculation and experiment, *Inorg. Chem. Front.*, 2023, **10**, 4711–4718.
  - 75 J. Li, Z. Lian, Q. Li, Z. Wang, L. Liu, F. L. Deepak, Y. Liu, B. Li, J. Xu and Z. Chen, Boosting acidic water oxidation performance by constructing arrays-like nanoporous  $\text{Ir}_x\text{Ru}_{1-x}\text{O}_2$  with abundant atomic steps, *Nano Res.*, 2022, **15**, 5933–5939.
  - 76 B. Zhang, X. Zhang, J. Yu, Y. Wang, K. Wu and M. Lee, First-principles high-throughput screening pipeline for



- nonlinear optical materials: application to borates, *Chem. Mater.*, 2020, **32**, 6772–6779.
- 77 G. Han, B. Lei, Z. Yang, Y. Wang and S. Pan, A fluorooxosilicophosphate with an unprecedented  $\text{SiO}_2\text{F}_4$  species, *Angew. Chem., Int. Ed.*, 2018, **57**, 9828–9832.
- 78 J. Zhou, Z. Fan, K. Zhang, Z. Yang, S. Pan and J. Li,  $\text{Rb}_2\text{CdSi}_4\text{S}_{10}$ : novel  $[\text{Si}_4\text{S}_{10}]$  T2-supertetrahedra-contained infrared nonlinear optical material with large band gap, *Mater. Horiz.*, 2023, **10**, 619–624.
- 79 L. Wang, C. Tu, H. Gao, J. Zhou, H. Wang, Z. Yang, S. Pan and J. Li, Clamping effect driven design and fabrication of new infrared birefringent materials with large optical anisotropy, *Sci. China: Chem.*, 2023, **66**, 1086–1093.